SCIENCE CHINA
Technological Sciences

• Article •

June 2016 Vol.59 No.6: 980–988
doi: 10.1007/s11431-016-6063-9

Hot deformation behaviour and processing maps of AA6061-10 vol.% SiC composite prepared by spark plasma sintering

LI XiaoPu[1*], LIU ChongYu[2*], SUN XiaoWei[3], MA MingZhen[1] & LIU RiPing[1]

[1] *State Key Laboratory of Metastable Materials Science and Technology, Yanshan University, Qinhuangdao 066004, China;*
[2] *Key Laboratory of New Processing Technology for Nonferrous Metal & Materials, Ministry of Education, Guilin University of Technology, Guilin 541004, China;*
[3] *Hebei Vocational and Technical College of Building Materials, Qinhuangdao 066004, China*

Received January 15, 2016; accepted April 20, 2016; published online May 13, 2016

AA6061-10 vol.% SiC composite was successfully prepared by spark plasma sintering. The deformation behaviour of this composite was studied using the uniaxial compression test, which was conducted at temperatures between 300 and 500°C and strain rates between 0.001 and 1 s^{-1}. Results indicate that the stress-strain curves of the AA6061-10 vol.% SiC composite typically feature dynamic recrystallization. The steady stress can be described by a hyperbolic sine constitutive equation, and the activation energy of the composite is 230.88 kJ/mol. The processing map was established according to the dynamic materials model. The optimum hot deformation temperature is 450–500°C and the strain rate is 1–0.1 s^{-1}. The instability zones of flow behaviour can also be identified using the processing map.

Al matrix composite, hot deformation, processing map, stress-strain curves, spark plasma sintering

Citation: Li X P, Liu C Y, Sun X W, et al. Hot deformation behaviour and processing maps of AA6061-10 vol.% SiC composite prepared by spark plasma sintering. Sci China Tech Sci, 2016, 59: 980–988, doi: 10.1007/s11431-016-6063-9

1 Introduction

High-performance and low-weight metal materials have attracted considerable attention because of the energy crisis and industrial demand. Aluminium-based metal matrix composites (AMMCs) have significant application potential in the aerospace, automotive, and electronics industries because of low cost, low density, high strength, high modulus, wear resistance, high thermal conductivity, and low thermal expansion coefficient [1–5].

Several methods are adopted to manufacture particle-reinforced AMMCs, such as stir casting, spray deposition, infiltration, and powder metallurgy [6–9]. The powder metallurgy has several desirable features compared with other preparation processes [10]. For example, powder metallurgy can produce AMMCs with uniformly distributed reinforcements because the fabrication process is not affected by the wettability of the reinforcements and Al. In addition, powder metallurgy can prevent undesirable reactions because of its low processing temperature and it can be utilised to design the volume fraction of reinforcement particles accurately [10]. Spark plasma sintering (SPS) is a rapid sintering technology that has gained considerable attention over the past few years. Compared with the conventional powder metallurgy techniques in the AMMCs manufacturing field, SPS exhibits faster heating rate, lower sintering temperature, and shorter sintering time. Its unique discharge technology can also play a role in cleaning and activating the surface of powders. Thus, SPS can maintain the original submicron and nanostructure of powder after sintering and can be adopted to obtain good interface bond-

---

*Corresponding authors (email: lxpcn@ysu.edu.cn; lcy261@glut.edu.cn)

© Science China Press and Springer-Verlag Berlin Heidelberg 2016

ing and fine grain composite material [11,12].

AMMCs prepared by powder metallurgy are usually processed by hot extrusion, hot forging, hot rolling, and other plastic processing technologies to improve the performance of AMMCs and to prepare various profiles [13]. However, the plastic processing of AMMCs is still difficult because of its high initial hardening rate, poor plasticity, and low elongation at room temperature [14]; thus, studying the hot deformation behaviour of AMMCs is pivotal. Although important investigations focusing on the deformation of AMMCs have been conducted, only a few have discussed the deformation behaviour of AMMCs prepared by SPS.

In this work, AA6061-SiC composites were prepared through ball milling and SPS. The hot deformation behaviour of the fabricated composites was further studied through isothermal and constant-strain-rate compression, which was conducted on a Gleeble-3500 testing system. The rheological properties of the composites under different strain rates and temperatures were evaluated. The constitutive equation was also established via kinetic analysis. Processing maps (PMs) were then established. Based on the PMs, the safe and unsafe operating zones were determined. Microstructural analysis was conducted to validate the results and to determine the deformation behaviour.

2 Experimental

The matrix material was composed of AA6061 alloy (Al-0.8Mg, 0.4Si, 0.1Mn, 0.1Cu, 0.2Zn, 0.06Cr, 0.2Ti, 0.7Fe) with a size of 400 mesh and the reinforcement was SiC particles (SiC_p) with a size of 15000 mesh. AA6061 (50 g) and SiC_p (6.4 g, 10 vol.%) were loaded in WC vials under an argon atmosphere and milled at RT in a planetary ball mill (Fritsch Pulverisette 4) using WC balls with a ball-to- sample weight ratio of 5:1. Milling was performed at 300 r/min for 2 h, and 1.5 mL ethanol was utilised as the process control agent to prevent the adhesion of aluminium powder.

To reduce oxidation, the mixture powder was formed in the glove box using a WC die with a diameter of 29.8 mm. The forming pressure is 150 MPa, and the relative density of the formed sample is approximately 70%. SPS was performed in a SPS-3.20MK-IV SPS system. The compaction pressure was 50 MPa, and the heating rate was 50°C/min. The sintering temperature and time were set at 560°C and 3 min, respectively. After SPS, the AA6061-SiC 10 vol.% composite with a diameter and height of 30 and 15 mm, respectively, was obtained.

Cylindrical compression specimens of φ10 × 15 mm were machined from the as-prepared (SPS) sample. The isothermal compression deformation test was performed at Gleeble3500-type-thermomechanical simulation test machine at different temperatures ranging from 300 to 500°C in steps of 50°C and various strain rates of 1, 0.1, 0.01, and 0.001 s^{-1} until the true strain of 0.7. All specimens were conductively heated to the specified temperature at a heating rate of 10°C/s and held at the temperature for 1 min to ensure that the temperature was homogeneous throughout the specimen. To reduce the influence of friction and ensure uniform deformation, a tantalum foil and lubricant was laid between the specimen and the anvil. All the specimens were quenched immediately to room temperature by water after the testing to preserve the microstructures deformed at high temperature.

The microstructure of the samples was observed using S-4800 scanning electron microscope (SEM), TM3030 tabletop SEM, and JEOL2100 transmission electron microscope (TEM). The SEM samples were etched for 30 s using Keller's reagent solution (2 mL HF, 3 mL HCl, 5 mL HNO_3, and 190 mL H_2O). The TEM specimens were prepared via ion milling. The electron backscatter diffraction (EBSD) was employed to analyse the grain size of as-SPSed samples. The EBSD samples were mechanical polished and electrolytic polished at 3 V for 1 s sequentially, the constituent of electrolyte solution is 190 mL CH_4O, 1.5 mL HNO_3, 5 mL $HClO_4$.

3 Results and discussion

3.1 Initial micro-morphology

The SEM images of the AA6061 and SiC_p in the present study are shown in Figure 1. It can be seen that the particle sizes of AA6061 alloy and SiC_p are about 10–30 μm and 0.2–0.5 μm, respectively, however, a few of large SiC_p with a maximum size of about 2 μm were observed in the low magnification image, as shown in Figure 1(b).

Figure 2 shows the SEM images of the AA6061-10 vol.% SiC mixture powder after 2 h of ball milling. The low magnification image indicates that the AA6061 powder was slightly deformed after milling (Figure 2(a)). Figure 2(b) illustrates the uniformly distributed SiC_p on the surface of the AA6061 powder.

Figure 3(a) describes the SEM images of the as-SPSed AA6061-10vol.%SiC composites. The grey and white regions corresponded to the AA6061 matrix and SiC_p layer, respectively. The morphology of AA6061 was not changed obviously during sintering. The SiC_p layer with a reticular structure distributed between aluminium alloy particles. EDS results indicate that the Al atom also exists in the SiC layer (Figure 3(b)).

Figure 3 shows that the sufficient densification structure with very few voids was obtained in the composite after spark plasma sintering at 560°C and 50 MPa for 3 min. Chen et al. [15] prepared an AA6061-B_4C composite with full densification via traditional vacuum hot pressing at 640°C under 120 MPa for 2.5 h, which indicates that SPS has a lower sintering temperature and a shorter sintering time.

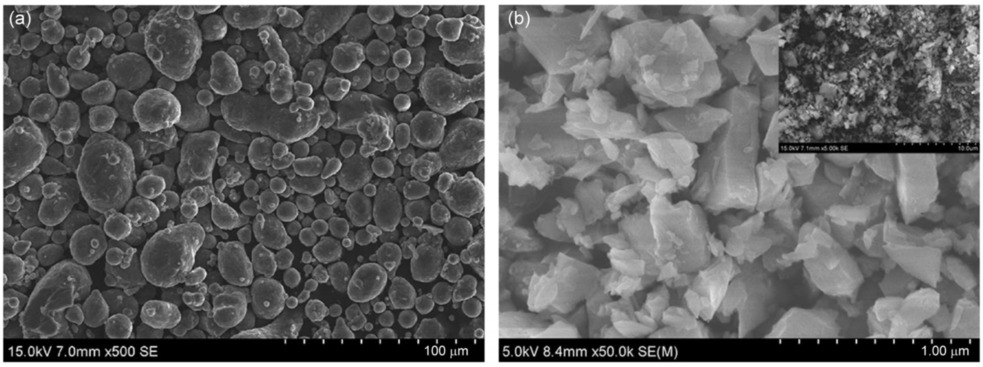

Figure 1 SEM images of the as-received (a) AA6061 and (b) SiC particles (low magnification inset).

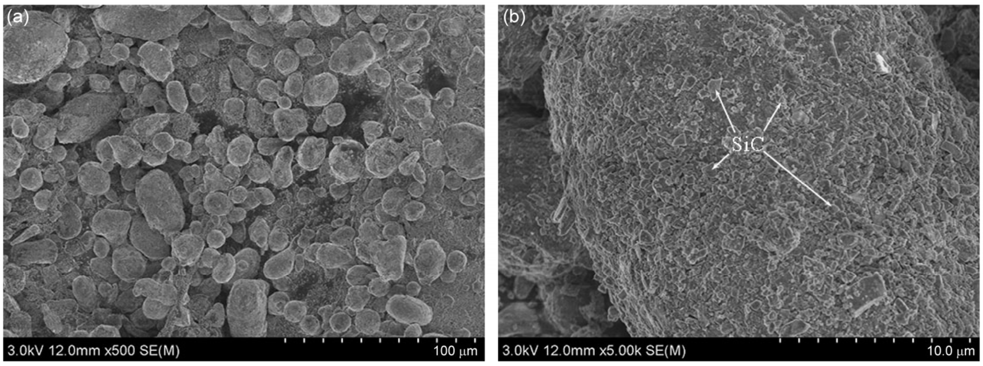

Figure 2 SEM images of AA6061-10 vol.% SiC powders after 2 h of ball milling: (a) low magnification; (b) high magnification.

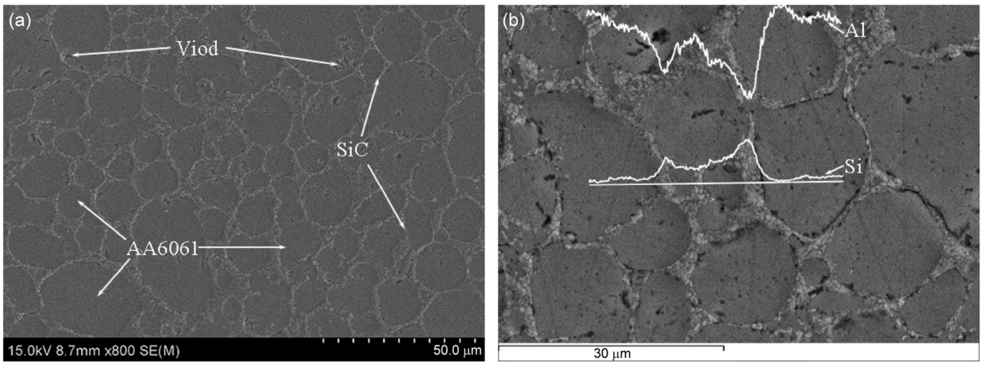

Figure 3 (a) SEM image of as-SPSed AA6061-10 vol.% SiC; (b) an enlarged SEM image and EDS line scan (inset).

The EBSD inverse pole figure (IPF) of AA6061 prepared by SPS at the same conditions is shown in Figure 4. The grain size of AA6061 is 0.65–29.67 μm and the average grain size is 9.4 μm according to the statistical analysis, which is much smaller than the grain size (80 μm) of AA2004-ZrB$_2$ prepared by stir casting [16].

3.2 True stress-true strain curves

Figure 5 presents the true stress–strain curves of the AA6061-10 vol.% SiC composite at different deformation conditions. The curves exhibit a rapid initial rise in stress and a monotonic decrease after attainment of peak stress. This occurs since the work hardening caused by the generation and multiplication of dislocation is being offset by dynamic flow softening after the peak stress. The features of the AA6061-10 vol.% SiC composite are typical characteristics of the dynamic recrystallization (DRX) process [17]. Figure 6(a) illustrates the microstructure of the AA6061-10 vol.% SiC composite with a deformation temperature of 500°C, strain rate of 1 s^{-1}, and strain of 0.1. A large number of dislocations that accumulate in the grains (particularly around the SiC$_p$) are evident in the image. Figure 6(b) presents the microstructure of the AA6061-10 vol.% SiC com-

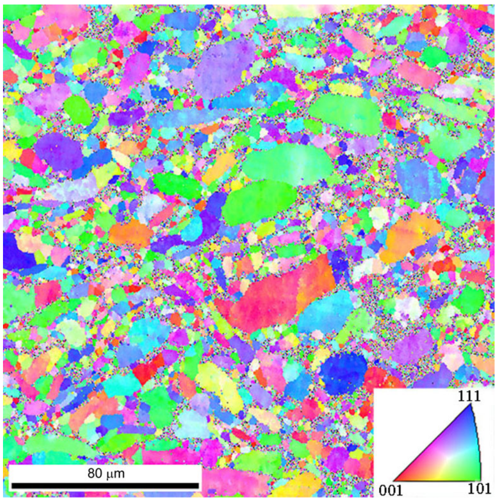

Figure 4 (Color online) EBSD IPF maps of AA6061 milled for 2 h and SPSed at 560°C, 50 MPa for 3 min.

posite with a deformation temperature of 500°C, strain rate of 1 s^{-1}, and strain of 0.5. Complete DRX grains can be observed. Based on the stress-strain curves, peak stress increased with strain rate. This phenomenon occurred because of the insufficient time for dislocation burgeoning and annihilation at higher strain rates and the DRX is incomplete, whereas the lower strain rate provides longer time for the nucleation of DRX [18]. Figure 5(a)–(e) indicates that peak stress value is reduced with the increase of deformation temperature. It is well documented that the increasing deformation temperature leads to the decreasing critical resolved shear stresses (CRSS) for basal and non-basal slip [19]. Besides, higher temperatures provide extra energy, which lead to the nucleation and growth of dynamically recrystallized grains and dislocation annihilation. Moreover, the adhesive strength between matrix and reinforcements decreases with the increase of temperature, and the load transfer effect from matrix to particle decreased. Thus, low

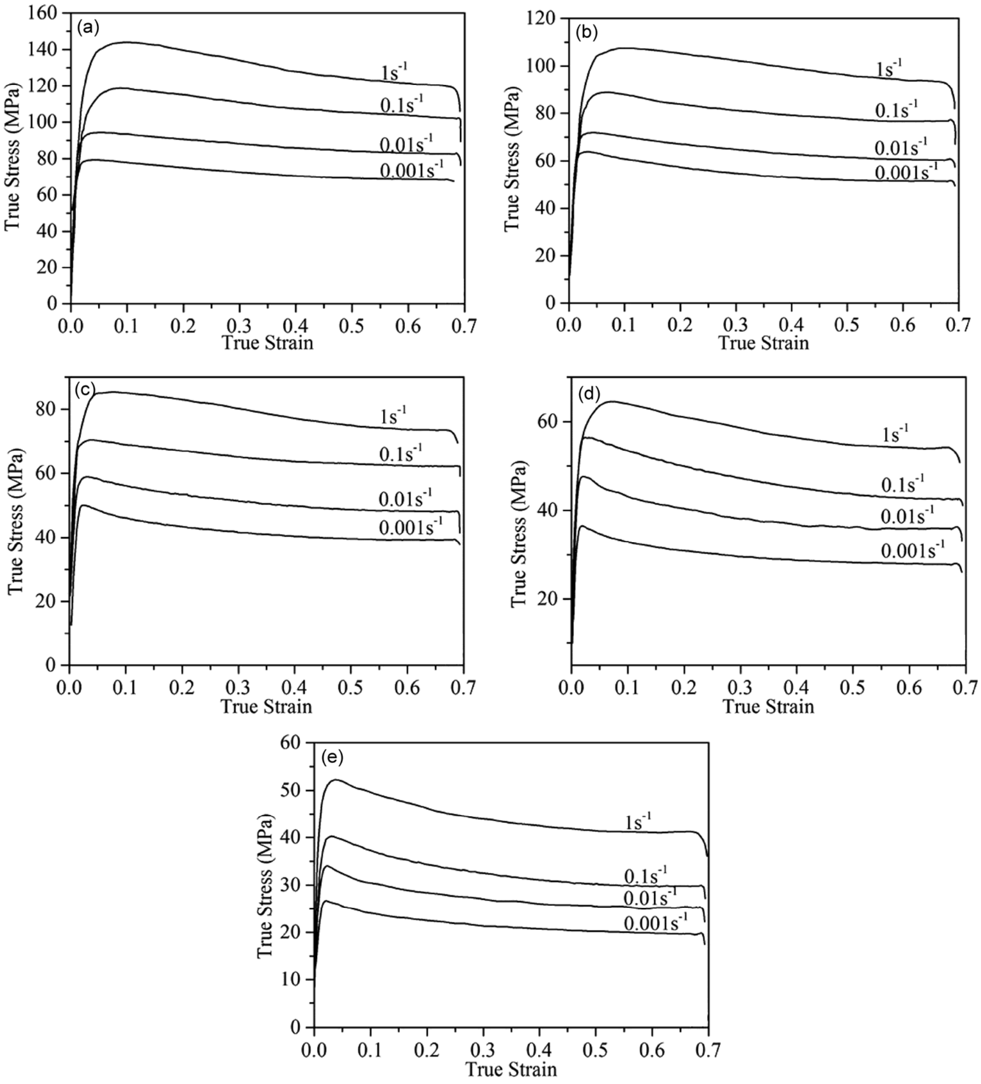

Figure 5 Flow stress-strain curves of the AA6061-10 vol.% SiC composite at different strain rates and temperature of (a) 300°C, (b) 350°C, (c) 400°C, (d) 450°C, and (e) 500°C.

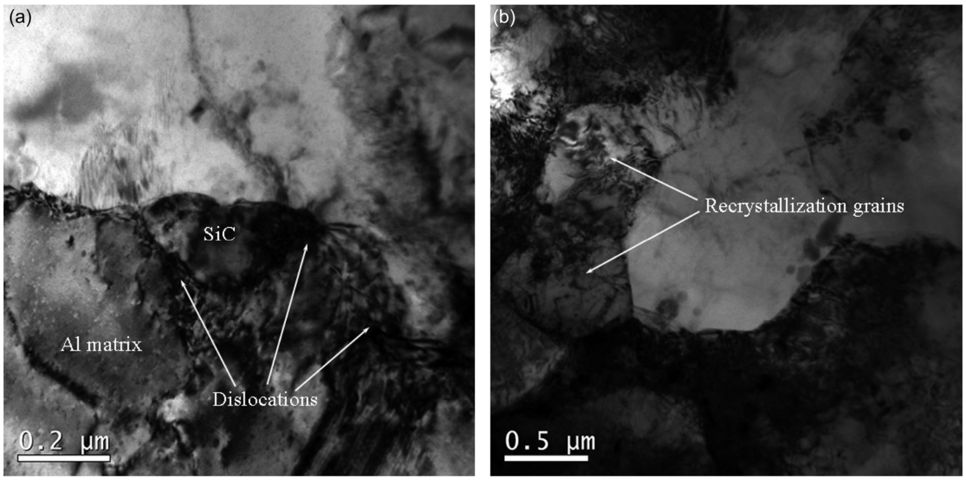

Figure 6 The bright field TEM images of the AA6061-10 vol.% SiC composite deformation at 500°C, strain rate of 1 s^{-1} with a strain of (a) 0.1 and (b) 0.5.

er CRSS, easier occurrence of DRX and lower load transfer effect may lead to the flow stress reducing at higher deformation temperatures [20–24].

3.3 Kinetic analysis

The deformation activation energy is an important kinetic parameter to describe the difficult degree of metal deformation. Eqs. (1) and (2) [25] are widely used to calculate the deformation activation energy at high temperature. The relationship between temperature, strain rate, and deformation activation energy was given by the Zener-Hollomon parameters in eq. (1). Eq. (2) describes the relationship between Z parameters and flow stress of metal.

$$Z = \dot{\varepsilon}\exp\left(\frac{Q}{RT}\right), \tag{1}$$

$$Z = A(\sinh(\alpha\sigma))^n. \tag{2}$$

Based on Arrhenius equations, Sellars and Mctegart [26] proposed a hyperbolic sine model that contains flow stress to describe deformation behaviour, as shown in eq. (3).

$$\dot{\varepsilon} = A(\sinh(\alpha\sigma))^n \exp\left(-\frac{Q}{RT}\right), \tag{3}$$

where A is a material constant; α is the stress adjustment factor; n is the stress exponent; $\dot{\varepsilon}$ is the strain rate; σ is the flow stress; Q is the activate energy; R is the gas constant (8.31 J mol^{-1} K^{-1}); T is the absolute temperature.

Based on eqs. (4) and (5), the values of n' and β were calculated from the slope of the $\ln\dot{\varepsilon}$-$\ln\sigma_p$ plot and $\ln\dot{\varepsilon}$-σ_p plot, respectively, by linear fitting. The two plots for the AA6061-10 vol.% SiC composite are presented in Figure 7(a) and (b), respectively. After determining the value of n' and β, α was computed using the relation $\alpha=\beta/n'$.

$$n' = \frac{\partial \ln\dot{\varepsilon}}{\partial \ln\sigma}, \tag{4}$$

$$\beta = \frac{\partial \ln\dot{\varepsilon}}{\partial \sigma}. \tag{5}$$

By considering the natural logarithm and differential on both sides of eq. (3), we obtain

$$Q = R\left[\frac{\partial \ln\dot{\varepsilon}}{\partial \ln(\sinh(\alpha\sigma))}\right]_T \left[\frac{\partial \ln(\sinh(\alpha\sigma))}{\partial(1/T)}\right]_{\dot{\varepsilon}}. \tag{6}$$

Figure 7(c) and (d) indicates the linear fitting plots of $\ln\dot{\varepsilon}$-$\ln(\sinh(\alpha\sigma_p))$ and $\ln(\sinh(\alpha\sigma_p))$-$1000/T$. By integrating the average value of the slopes obtained from the fitting into eq. (6), the average deformation activation energy Q was calculated to be 230.88 kJ/mol, which is significantly higher than that of 196 kJ/mol for AA6061 [27]. The higher Q value in the composite is due to the effect of ultrafine SiC_p which pins the motion of the dislocations and grain boundaries and raises the resistance stress of deformation. This value is also higher than that for AA6061-15% SiC_p (215 kJ/mol) [28] and AA6061-20% SiC (195 kJ/mol) [29]. This may be attributed to the finer reinforcements and the higher strain rates in the present study. It is reported that the self-diffusion activation energy of aluminium matrix is 144 kJ/mol [30]. Kai and Chen et al. [31,32] noted that dynamic recrystallization or dynamic recovery dominated the deformation mechanism instead of diffusion, when the activation energy is greater than that of the lattice self-diffusion. In fact, it is because the blocking effect of the fine SiC_p on the dislocation motion, which leads to the accumulation of dislocations in the vicinity of SiC_p, that result in the occurrence of DRX.

Considering the natural logarithm on both sides of eq. (2), we obtain

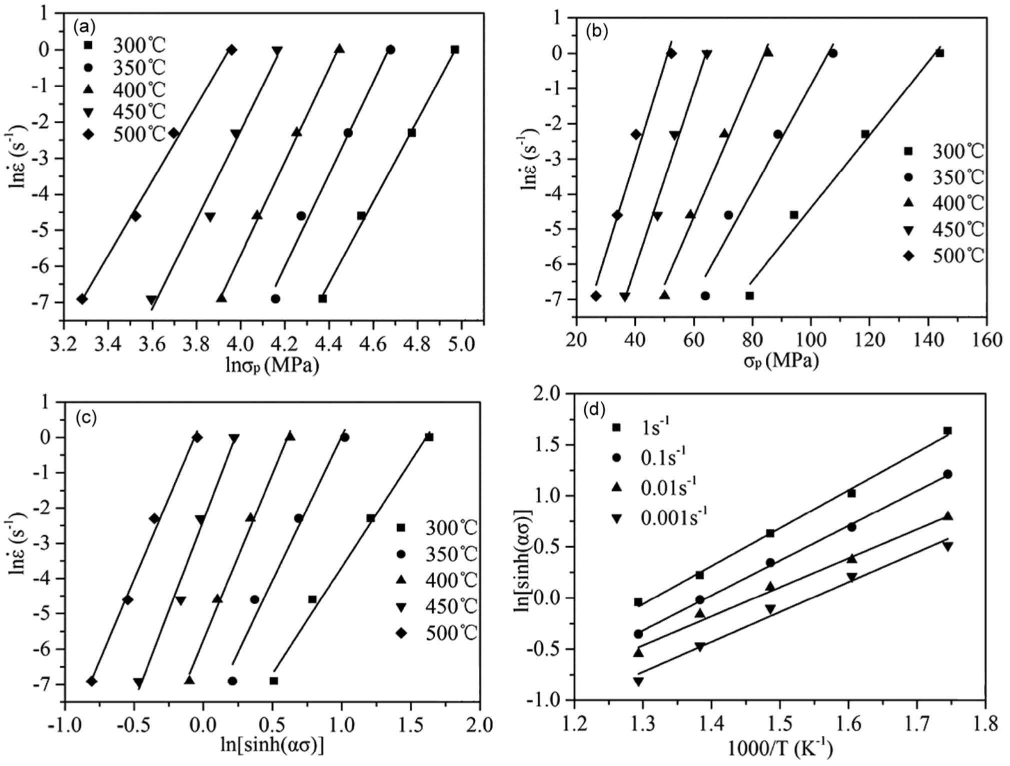

Figure 7 Linear fitting plots of (a) $\ln\dot{\varepsilon}$ –lnσ_p; (b) $\ln\dot{\varepsilon}$ –σ_p; (c) $\ln\dot{\varepsilon}$ –ln(sinh($\alpha\sigma_p$)); (d) ln(sinh($\alpha\sigma_p$))-1000/*T*.

$$\ln Z=\ln A+n\ln(\sin(\alpha\sigma)). \tag{7}$$

By substituting the values of *Q*, *α*, and *σ* into eq. (1), the value of ln*Z* was calculated, as shown in Table 1. Considering eq. (7) and the linear fitting plot of ln*Z*-ln(sinh($\alpha\sigma_p$)), as illustrated in Figure 8, the slope of the fitting line was *n* and the intercept was ln*A*. According to the fitting results, n=8.44, A=4.58x10^{15}, and the correlation coefficient was 0.98. Thus, the hot deformation behaviour of the AA6061-10 vol.% SiC composite can be described by the hyperbolic sine model as

$$\dot{\varepsilon}=4.58\times10^{15}\times(\sinh(0.01623\sigma))^{8.44}\times\exp\left(-\frac{230.88\times10^{3}}{RT}\right). \tag{8}$$

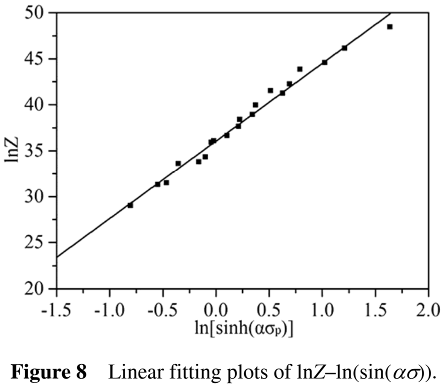

Figure 8 Linear fitting plots of ln*Z*–ln(sin($\alpha\sigma$)).

Table 1 indicates that the value of *Z* increases with strain rate and all the higher *Z* values correspond to the lower deformation temperature, indicating a higher degree of work hardening at a low temperature [33]; the *Z* value decreases with deformation temperature because of dynamic softening [34,35].

3.4 Processing maps

PMs based on the dynamic materials model were widely used in the industrial field as a powerful tool to determine optimum plastic processing parameters [36]. PMs are developed by superimposing the instability map on the power dissipation map. The power dissipation map represents power dissipation through microstructure changes, which is expressed by power dissipation efficiency *η*, as given by eq. (9) [37].

Table 1 ln*Z* at different temperatures and strain rates

Temperature (°C)	ln*Z* under different deformation conditions (s^{-1})			
	1	0.1	0.01	0.001
300	48.46	46.16	43.86	41.56
350	44.57	42.27	39.97	37.67
400	41.26	38.96	36.66	34.36
450	38.41	36.11	33.80	31.50
500	35.93	33.62	31.32	29.02

$$\eta = \frac{2m}{m+1}, \tag{9}$$

where m is the strain rate sensitivity coefficient. Its value can be obtained by adopting three polynomial fittings of the plot of $\ln\sigma$–$\ln\dot{\varepsilon}$, as indicated in eq. (10) [38]:

$$m = \left.\frac{\partial \ln \sigma}{\partial \ln \dot{\varepsilon}}\right|_{\varepsilon, T}. \tag{10}$$

The flow-instability map represents the continuum instability criterion based on the principles of irreversible thermodynamics caused by large plastic flows [39]. Instability is numerically represented by a dimensionless parameter ξ, as shown in eq. (11). The condition $\xi(\dot{\varepsilon})<0$ represents the instability region. The variation of ξ with strain rate and temperature provides the instability map.

$$\xi(\dot{\varepsilon}) = \frac{\partial\left[m/(m+1)\right]}{\partial \ln \dot{\varepsilon}} + m. \tag{11}$$

Based on eqs. (9)–(11) and the flow stress data obtained in the isothermal compression tests, the PMs at strain levels of 0.2, 0.4, and 0.6 were constructed, as illustrated in Figure 9. The contour numbers represent the power dissipation efficiency. Higher η values denote the better processing properties of the composites. The darker shaded region indicates the instability zone.

Evidently, all the PMs with different strains exhibit two instability zones, and the instability zones increase with strain. Two extreme value areas of power dissipation efficiency were observed at (1) around 500°C and 1 s^{-1} and (2) 450°C and 0.001 s^{-1}. At a strain levels of 0.6, the instability zones were in the (1) temperature range of 300–440°C and strain rate range of 1–0.1 s^{-1} and (2) temperature range of 440–500°C and strain rate range of 0.01–0.001 s^{-1}. However, the second instability zones overlap on the second extreme area of η. Thus, the optimum hot deformation condition of the AA6061-10 vol.% SiC composite was at 450–500°C and 1–0.1 s^{-1}.

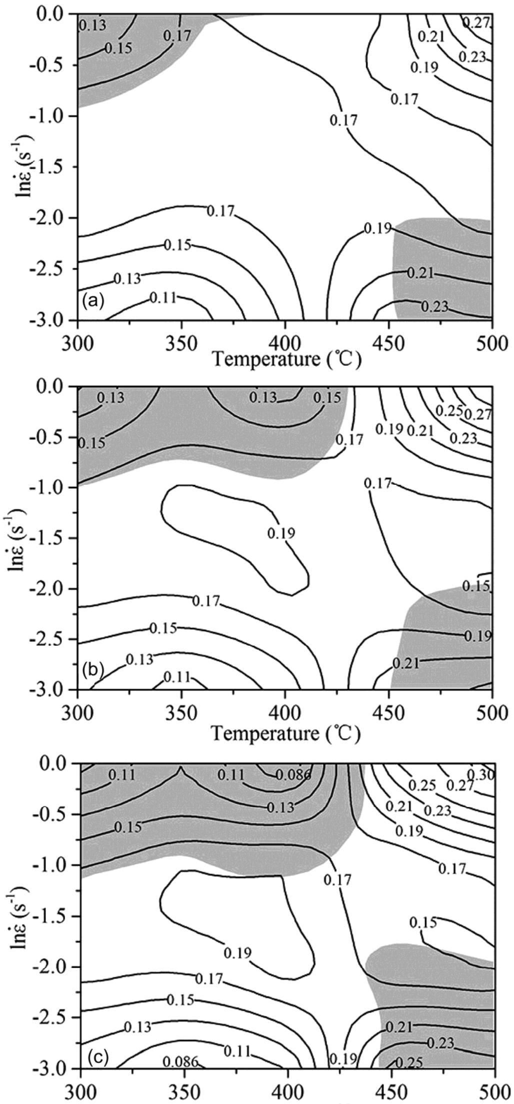

Figure 9 Processing maps at strain levels of (a) 0.2, (b) 0.4, (c) 0.6.

3.5 Microstructure evolution

Figure 10 presents the microstructure of the AA6061-10 vol.% SiC composite at different deformation conditions. In Figure 10(a), the AA6061 particles exhibited an elongated “pancake” structure, the SiC layer was continuously distributed at the AA6061 particle boundaries with a reticular structure, and serious flow localization was observed at 300°C and 1 s^{-1}. In this condition, the matrix and SiC particles were significantly uncoordinated, and the deformability of the composite was poor. Thus, the localised stress concentration caused flow localization and resulted in deformation instability [40]. When the strain rate decreased to 0.001 s^{-1}, flow localization disappeared, AA6061 particles exhibited a uniform “pancake” shaped structure, and the SiC layer was discontinuously arranged, as shown in Figure 10(b). When the deformation temperature increases to 500°C, the “pancake” AA6061 particles disappear and the SiC layer further diffuses into a punctate distribution, as shown in Figure 10(c). Meanwhile, as shown in Figure 10(d), substantial cracks appear in the microstructure at a stain rate 0.001 s^{-1}, which may be related to abnormal grain growth [41].

The TEM investigations were performed to reveal the microstructural features of composites after deformation, as shown in Figure 11. Figure 11(a) shows the grains are elongated and contain a few recrystallized subgrains, indicating an uncompleted DRX was occurred in the sample during hot deformation at 300°C. Figure 11(b) shows that DRX is complete in the AA6061-10 vol.% SiC composite at 500°C deformation temperature when the true strain reaches 0.7. Doherty’s [42] investigation illustrates that a region of

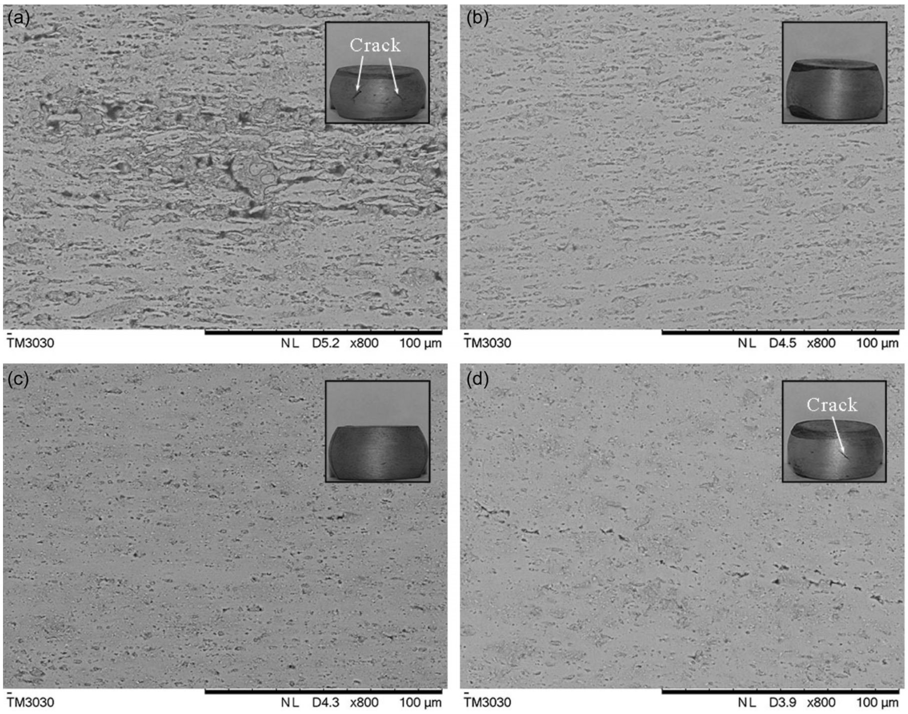

Figure 10 The SEM images and optical images (inset) of the AA6061-10vol.%SiC composite at different deformation conditions: (a) 300 °C, 1 s^{-1}; (b) 300°C, 0.001 s^{-1}; (c) 500°C, 1 s^{-1}; (d) 500°C, 0.001 s^{-1}.

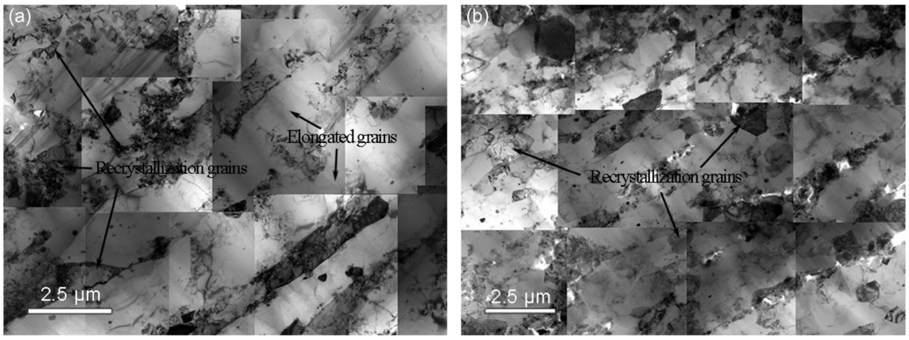

Figure 11 The BF TEM images of the AA6061–10vol.%SiC composite at different deformation conditions: (a) 300°C, 0.001 s^{-1}; (b) 500°C, 1 s^{-1}.

high dislocation density and large orientation gradient is created by the enforced strain gradient in the vicinity of a non-deforming particle during the deformation process. This region is called particle deformation zone (PDZ), which is an ideal site for development of a recrystallization nucleus [43]. Consequently, the existence of PDZ around fine SiC_p particles and the high deformation temperature promote the occurrence of fully DRX in the AA6061-10 vol.% SiC composite during hot deformation at 500°C.

4 Conclusions

The AA6061-10 vol.% SiC composite was prepared by ball milling and SPS. The hot deformation behaviour of the composite was studied at a deformation temperature of 300–500°C and strain rate of 0.001–1 s^{-1}. The following conclusions are drawn from the results.

1) The AA6061-10 vol.% SiC composite with sufficient densification was prepared by SPS at 560°C under 50 MPa. The peak stress of the AA6061-10 vol.% SiC composite during hot deformation is reduced along with the increase in temperature and decrease in strain rate.

2) The average deformation activation energy for the AA6061-10 vol.% SiC composite was 230.88 kJ/mol, which is higher than that for AA6061 and the self-diffusion activation energy for aluminium. The constitutive equation of the composite was established as

$$\dot{\varepsilon}=4.58\times10^{15}\times(\sinh(0.01623\sigma))^{8.44}\times\exp(-230.88\times10^{3}/RT).$$

3) Two instability zones in the PMs of the AA6061-10vol.%SiC composite were identified: (1) 300–440°C,

1–0.1 s^{-1} and (2) 440–500°C, 0.01–0.001 s^{-1}. Two extreme value areas of power dissipation efficiency were determined as follows: (1) at approximately 500°C and 1 s^{-1} and (2) at 450°C and 0.001 s^{-1}. The PMs and microstructural analysis indicated that the optimal processing conditions of the AA6061-10 vol.% SiC composite were 450–500°C and 1–0.1 s^{-1}.

This work was supported by the National Basic Research Program of China ("973" Project) (Grant No. 2013CB733000).

1 Liu C Y, Wang Q, Jia Y Z, et al. Evaluation of mechanical properties of 1060-Al reinforced with WC particles via warm accumulative roll bonding process. Mater Des, 2013, 43: 367–372

2 Sahin Y. Preparation and some properties of SiC particle reinforced aluminum alloy composites. Mater Des, 2003, 24: 671–679

3 Suraj P R. Metal-matrix composites for space applications. JOM, 2001, 53: 14–17

4 Koli D K, Agnihotri G, Purohit R. Advanced aluminium matrix composites: The critical need of automotive and aerospace engineering fields. Mater Today, 2015, 2: 3032–3041

5 Surappa M K. Aluminum matrix composites: Challenges and opportunities. Sadhana, 2003, 28: 319–334

6 Gopalakrishnan S, Murugan N. Production and wear characterisation of AA 6061 matrix titanium carbide particulate reinforced composite by enhanced stir casting method. Compos Part B-Eng, 2012, 43: 302–308

7 Frank S Y H, Chen Y C, Tsao C Y A. Workability of spray-formed 7075 Al alloy reinforced with SiC$_p$ at elevated temperatures. Mat Sci Eng A-Struct, 2004, 364: 296–304

8 Zhang Q, Ma X Y, Wu G H. Interfacial microstructure of SiC$_p$/Al composite produced by the pressureless infiltration technique. Ceram Int, 2013, 39: 4893–4897

9 Zhang J T, Liu L S, Zhai P C, et al. Effect of fabrication process on the microstructure and dynamic compressive properties of SiC$_p$/Al composites fabricated by spark plasma sintering. Mater Lett, 2008, 62: 443–446

10 Lloyd D J. Particle reinforced aluminum and magnesium matrix composites. Int Mater Rev, 1994, 39: 1–23

11 Orrù R, Licheri R, Locci A M, et al. Consolidation/synthesis of materials by electric current activated/assisted Sintering. Mater Sci Eng R, 2009, 63: 127–287

12 Song X Y, Liu X M, Zhang J X. Mechanism of conductive powder microstructure evolution in the process of SPS. Sci China Ser E-Tech Sci, 2005, 48: 258–269

13 Zabihi M, Toroghinejad M R, Shafyei A. Application of powder metallurgy and hot rolling processes for manufacturing aluminum/alumina composite strips. Mat Sci Eng A-Struct, 2013, 560: 567–574

14 El-Sabbagha A, Solimanb M, Tahaa M, et al. Hot rolling behaviour of stir-cast Al 6061 and Al 6082 alloys-SiC fine particulates reinforced composites. J Mater Process Tech, 2012, 212: 497–508

15 Chen H S, Wang W X, Li Y L, et al. The design, microstructure and tensile properties of B$_4$C particulate reinforced 6061Al neutron absorber composites. J Alloys Compd, 2015, 632: 23–29

16 Kai X Z, Zhao Y T, Wang A D, et al. Hot deformation behavior of *in situ* nano ZrB$_2$ reinforced 2024Al matrix composite. Compos Sci Technol, 2015, 116: 1–8

17 Saravanan L, Senthilvelan T. Investigations on the hot workability characteristics and deformation mechanisms of aluminium alloy-Al$_2$O$_3$ nanocomposite. Mater Des, 2015, 79: 6–14

18 Wu B, Li M Q, Ma D W. The flow behavior and constitutive equations in isothermal compression of 7050 aluminum alloy. Mat Sci Eng A-Struct, 2012, 542: 79–87

19 Wang X J, Wu K, Huang W X, et al. Study on fracture behavior of particulate reinforced magnesium matrix composite using *in situ* SEM. Compos Sci Technol, 2007, 67: 2253–2260

20 Ganesan G, Raghukandan K, Karthikeyan R, et al. Formability study on Al/SiC composites. Mater Sci Forum, 2003, 437/438: 227–230

21 Zhang P, Li F G, Wan Q. Constitutive equation and processing map for hot deformation of SiC particles reinforced metal matrix composites. J Mater Eng Performan, 2010, 19: 1290–1297

22 Zhang H, Lin G Y, Peng D S, et al. Dynamic and static softening behaviors of aluminum alloys during multistage hot deformation. J Mater Process Tech, 2004, 148: 245–249

23 Li H Z, Wang H J, Zeng M, et al. Forming behavior and workability of 6061/B$_4$C$_p$ composite during hot deformation. Compos Sci Technol, 2011, 71: 925–930

24 Yar A A, Montazerian M, Abdizadeh H, et al. Microstructure and mechanical properties of aluminum alloy matrix composite reinforced with nano-particle MgO. J Alloys Compd, 2009, 484: 400–404

25 Jin N P, Zhang H, Han Y, et al. Hot deformation behavior of 7150 aluminum alloy during compression at elevated temperature. Mater Charact, 2009, 60: 530–536

26 Sellars C M, Mctegart W J. On the mechanism of hot deformation. Acta Metall, 1966, 14: 1136–1138

27 Khamei A A, Dehghani K. Hot ductility of severe plastic deformed AA6061 aluminum alloy. Acta Metall Sin (English Lett), 2015, 28: 322–330

28 Ganesan G, Raghukandan K, Karthikeyan R, et al. Development of processing maps for 6061 Al/15% SiC$_p$ composite material. Mat Sci Eng A-Struct, 2004, 369: 230–235

29 Asgharzadeh H, Simchi A. Hot Deformation Behavior of P/M Al6061-20% SiC Composite. Mater Sci Forum, 2007, 534: 897–900

30 Sohn Y. Diffusion in Metals. In: Gale W F, Totemeir T C, eds. Smithells Metals Reference Book. 8th ed. Oxford: Elsevier Butterworth-Heinemann, 2004. 13-11

31 Kai X Z, Zhao Y T, Wang A D, et al. Hot deformation behavior of *in situ* nano ZrB$_2$ reinforced 2024Al matrix composite. Compos Sci Technol, 2015, 116: 1–8

32 Chen W, Guan Y P, Wang Z H. Hot deformation behavior of high Ti 6061 Al alloy. T Nonferr Metal Soc China, 2016, 26: 369–377

33 Rajamuthamilselvan M, Ramanathan S, Karthikeyan R. Processing map for hot working of SiC$_p$/7075 Al composites. T Nonferr Metal Soc China, 2010, 20: 668–674

34 Li J, Li F G, Cai J, et al. Flow behavior modeling of the 7050 aluminum alloy at elevated temperatures considering the compensation of strain. Mater Des, 2012, 42: 369–377

35 Zhang F, Shen J, Yan X D, et al. High-temperature flow behavior modeling of 2099 alloy considering strain effects. T Nonferr Metal Soc China, 2014, 24: 798–805

36 Prasad Y V R K, Rao K P, Hort N, et al. Optimum parameters and rate controlling mechanisms for hot working of extruded Mg-3Sn-1Ca alloy. Mater Sci Eng A, 2009, 502: 25–31

37 Prasad Y V R K, Rao K P, Sasidhara S. Hot Working Guide: A Compendium of Processing Maps. 2nd ed. Materials Park: ASM International, 2015. 5–6

38 Prasad Y V R K, Gegel H L, Doraivelu S M, et al. Modeling of dynamic material behavior in hot deformation: Forging of Ti-6242. Metall Mater Trans A, 1984, 15: 1883–1892

39 Ziegler H. Some Extremum Principles in Irreversible Thermodynamics with Application to Continuum Mechanics. In: Sneddon I N, Hill R, eds. Progress in Solid Mechanics Vol. 4. New York: Interscience Publishers Inc., 1965. 191–193

40 Zhong T, Rao K P, Prasad Y V R K, et al. Processing maps, microstructure evolution and deformation mechanisms of extruded AZ31-DMD during hot uniaxial compression. Mat Sci Eng A-Struct, 2013, 559: 773–781

41 Jiang F L, Zhang H, Ji X K, et al. Comparative hot deformation characters of Al-Mn-Mg-Re alloy and Al-Mn-Mg-Re-Ti alloy. Mat Sci Eng A-Struct, 2014, 595: 10–17

42 Doherty R D, Hughes D A, Humphreys F J, et al. Current issues in recrystallization: a review. Mat Sci Eng A-Struct, 1997, 238: 219–74

43 Ahamed H, Senthilkumar V, Hot deformation behavior of mechanically alloyed Al6063/0.75Al$_2$O$_3$/0.75Y$_2$O$_3$ nano-composite—a study using constitutive modeling and processing map. Mat Sci Eng A-Struct, 2012, 539: 349–359